ceramics

MDPI

Article

A Facile Method Using a Flux to Improve Quantum Efficiency of Submicron Particle Sized Phosphors for Solid-State Lighting Applications

Jungmin Ha [1], Ekaterina Novitskaya [2], Gustavo A. Hirata [3], Chenhui Zhou [4], Robyn E. Ridley [1], Olivia A. Graeve [1,2] and Joanna McKittrick [1,2,*]

1 Materials Science and Engineering Program, University of California, San Diego, 9500 Gilman Dr., La Jolla, CA 92093, USA; jungminha@eng.ucsd.edu (J.H.); reridley@ucsd.edu (R.E.R.); ograeve@eng.ucsd.edu (O.A.G.)
2 Department of Mechanical and Aerospace Engineering, University of California, San Diego, 9500 Gilman Dr., La Jolla, CA 92093, USA; eevdokim@ucsd.edu
3 Center for Nanoscience and Nanotechnology, 22860 Ensenada, Mexico; hirata@cnyn.unam.mx
4 Department of Chemical Engineering, University of California, San Diego, 9500 Gilman Dr., La Jolla, CA 92093, USA ; c2zhou@ucsd.edu
* Correspondence: jmckittrick@ucsd.edu; Tel.: +1-858-534-5425; Fax: +1-858-534-5698

Received: 17 May 2018; Accepted: 6 June 2018; Published: 8 June 2018

Abstract: This work successfully verified that the addition of a flux (NH_4F, NH_4Cl, and H_3BO_3) during synthesis has an impact on the crystallite size and quantum efficiency of submicron-sized particles of $CaMgSi_2O_6$:Eu^{2+} phosphors. The addition of NH_4F or NH_4Cl increased the crystallite size in the submicron-sized particles, yielding an increase in emission intensity and quantum efficiency. On the other hand, the use of the H_3BO_3 flux crystallized a secondary phase, SiO_2, and changed the lattice parameters, which degraded the luminescent properties. In addition, an excessive amount of NH_4Cl was examined, resulting in nucleation of a secondary phase, $CaSiO_3$, which changed the lattice parameters with no improvement in luminescent properties. These results demonstrate that the addition of a flux could be a method to improve the quantum efficiency of submicron-sized particles composed of nanocrystallites; however, a judicious choice of the flux composition and amount has to be carefully considered.

Keywords: phosphors; Eu^{2+} activation; flux; quantum efficiency; crystallite size

1. Introduction

Powder phosphors produced by the conventional solid-state reaction method have been widely researched for application in near UV-emitting LEDs (nUV-LEDs) [1,2]. This method produces micron-sized powders that have higher quantum efficiencies than smaller-sized powders [3,4], whereas chemical synthesis methods produce submicron-sized powders composed of nanocrystallites. Particle size and crystallite size should be differentiated to understand the quantum efficiency of phosphors. A powder particle can be a single crystal or consist of crystallites, the crystallite size is typically measured by X-ray diffraction or transmission electron microscopy, whereas the particle size is typically measured by dynamic light scattering or scanning electron microscopy. In the remote phosphor configuration, the phosphor particles are on a substrate that is suspended above a nUV-LEDs, as opposed to the conventional configuration where the phosphors are embedded in a polymer around a blue-emitting LED. In addition, in the remote configuration, the packing density of the large particles is low, which generates substantial light scattering [5]. To overcome this issue, phosphors with a small, narrow particle size distribution are required. If the particle radii are <~400 nm, these particles will

negligibly scatter visible and near UV radiation, because particle size is smaller than the wavelength of the radiation. However, phosphor particles in the submicron-size regime with nano-sized crystallites have poor quantum efficiency compared to micrometer-sized, single crystal phosphor particles [2,6].

One method that is used to improve the crystallinity and quantum efficiency of micrometer-sized particles is to use a flux [7–9]. A flux material is an inert high-temperature solvent used to accelerate crystallite growth. Generally, 0.5 wt.%~10 wt.% of a flux is used [8,10], forming a thin layer of molten material around crystals during the annealing process and facilitating a high diffusivity path through the flux [10]. Crystals grow in the molten salt solvents, thus normally called flux growth. The process is a well-known method for crystal growth in materials [1,11,12]. A flux is typically used in preparing phosphor powders through a solid-state reaction method, producing regular-shaped particles and enlarged crystallites, which cause the emission intensity to be enhanced [7–9,13–17]. However, this process is rarely researched for nanocrystalline, submicrometer-sized phosphors prepared by wet chemical processes [18–21]. Table 1 shows the effect of various flux compositions on phosphor properties for application in nUV-LED lighting [7–9,13–21]. In each case, the phosphor properties (e.g., quantum efficiency, particle size and surface smoothness) were enhanced with the addition of a flux. In fact, after adding a flux, aluminates and oxides showed enlarged particles and smooth particle surfaces [7,8,15,18], silicates and oxy-nitrides have larger crystallite sizes and regular particle morphology [14,16,19,20]. Most importantly, these phosphors all have enhanced emission intensity or quantum efficiencies with the addition of a flux.

A flux is typically mixed with reactants [7,8,14–16,19] or as-synthesized product [20] before an annealing step; thus, is present as the molten phase during the post-synthesis annealing process. Since the flux material should be evaporated after annealing to avoid formation of impurities or second phases in the final product, the melting and boiling temperatures should be considered in relationship to the annealing conditions (temperature, atmosphere), when selecting a flux material. The criteria for selecting a flux are: (1) a low melting temperature, so that it is a liquid during the annealing process [9]; (2) a boiling temperature lower than the annealing temperature, so that the flux can be evaporated to avoid impurity or a second phase formation [13]. Fluxes having a higher boiling temperature than the annealing temperature had been used in most of the previous literature (Table 1); and (3) the difference in ionic radii of the flux and the phosphor elements must be more than 30% to avoid doping of the flux elements in the phosphors [22]. Chiang et al. [7] reported a formation of a second phase of $BaAl_2O_4$ in $Y_{2.95}Ce_{0.05}Al_5O_{12}$ with a BaF flux. This suggests that some fluxes can remain after the reaction, producing by-products.

Dai et al. [9] discussed the effect of various fluxes (NH_4Cl, NH_4F, H_3BO_3, LiF, and NaF) on the emission intensity of $Y_{1.55}Eu(III)_{0.45}Ti_2O_7$ phosphors with an orange-red emission under near UV light for display devices such as high-resolution and field emission displays, as well as high-power white light-emitting diodes. It was found that uniform micrometer-sized (~4 μm) particles formed with NaF and LiF fluxes, and the maximum emission intensity was achieved with NaF flux, while a narrow size distribution of the particles was not achieved with NH_4Cl, NH_4F, or H_3BO_3 fluxes. Additionally, Zhang et al. [8] examined the influence of different concentrations of BaF_2 flux on the formation of $Ca_{0.99}Ce_{0.01}Sc_2O_4$ with green emission prepared by a solid-state reaction. After introducing BaF_2, a higher particle growth rate, larger particle sizes, and more narrow particle size distribution were verified, which resulted in improved emission intensity. The emission intensity increased with the increase of the concentration of BaF_2 and the maximum emission intensity corresponded to 0.5 wt.% of BaF_2. The emission intensity decreased when the concentration of BaF_2 was higher than 0.5 wt.%, which was attributed to particle agglomeration. Wang et al. [20] examined the effect of Li_2CO_3 and K_2CO_3 fluxes on the formation of $Ca_{0.68}Mg_{0.2}Eu_{0.12}SiO_3$ prepared by a co-precipitation method. The crystallite size increased from ~93 nm to 99 nm (6% of Li_2CO_3) or to 100 nm (5% of K_2CO_3), and the quantum efficiencies were improved (from 12% to 27% with Li_2CO_3 flux and to 31% with K_2CO_3 flux).

Table 1. Reported results of the addition of flux on phosphor preparation. T_m = melting temperature, T_b = boiling temperature, Φ = quantum efficiency.

Flux/T_m/T_b (°C)	Phosphor Composition	Synthesis Method	Annealing Temperature (°C)	Results	Ref.
CaF_2/1418/2533	$(Ca_{0.99}Ce_{0.01})_3Sc_2Si_3O_{12}$	Solid state reaction	1100–1450	Reduced impurities, decreased formation temperature, no reported crystallite size and Φ, emission intensity increased 2×, narrow particles distribution, removed flux by sublimation after reaction	[13]
BaF_2/1368/2260	$Y_{2.965}Ce_{0.035}Al_5O_{12}$	Spray pyrolysis	1300–1600	Enlarged, regular morphology, and non-aggregated particles, no reported crystallite size and Φ, emission intensity increased 1.4×	[18]
	$Y_{2.95}Ce_{0.05}Al_5O_{12}$	Solid state reaction	1000–1500	Able to reduce annealing temperature $BaAl_2O_4$, byproduct from BaF_2 Spherical shape and smooth surface Φ external) increased 1.3× over commercial sample	[7]
	$Ba_{0.85}Eu_{0.15}Si_3Al_3O_4N_5$	Solid state reaction	1550	Enlarged crystallite size (no specific number) and particles size, narrow particles distribution, emission intensity increased slightly, no reported Φ	[14]
	$Ca_{0.99}Ce_{0.01}Sc_2O_4$	Solid state reaction	1550 and 1450	Φ external) increased 1.1×, no reported crystallite size, enlarged and regular particles	[8]
LiF/845/1673	$Ba_{0.9}Eu_{0.1}Mg_{0.98}Mn_{0.02}Al_{10}O_{17}$	Molten salt synthesis	1100–1400	Particles size enlarged, Li^+ into the host lattice analyzed by lattice parameter, no report crystallite size from XRD, no reported Φ, emission intensity increased 2×	[15]
NaF/993/1695	$Lu_{2.925}Ce_{0.075}Al_{4.79}Si_{0.21}O_{11.79}N_{0.21}$	Solid state reaction	1500	Emission intensity increased 1.3×, regular morphology of particles, no report crystallite size and Φ	[16]
NaF/993/1695 LiF/845/1675 H_3BO_3/171/300 NH_4F/100/decomposes	$Y_{1.55}Eu_{0.45}Ti_2O_7$	Solid state reaction	1350	Crystallite size enlarged (no specific number), emission intensity increased 11× (NaF), 9× (LiF), 5× (H_3BO_3), 2.5× (NH_4F), 39% of Φ (NaF), no reported Φ without flux, enlarged particles size	[9]
NH_4Cl/338/decomposes	$Ba_{1.488}Sr_{0.5}Eu_{0.012}SiO_4$	Spray pyrolysis	900–1400	Enlarged particles, enlarged crystallite size (no specific number), no reported Φ, emission intensity increased 1.3×, optimum annealing temperature decreased	[19]
K_2CO_3/891/decomposes	$Ca_{0.68}Eu_{0.12}Mg_{0.2}SiO_3$	Co-precipitation	1200	Charge compensation, crystallite size increased 1.1×, Φ increased 2.5×, no phase composition change, no reported particles size	[20]
Li_2CO_3/734/1310	$(Sr_{0.92}Eu_{0.08})_8Al_{12}O_{24}S_2$	Solid state reaction	900	Improved purity, but still impurities remained. No report crystallite size and Φ	[17]
$SrCl_2$/874/1250	$Sr_{1.56}Eu_{0.04}Ba_{0.4}SiO_4$	Combustion	800–950	Crystallite size increased (no specific number), emission intensity increased 2.7×, no reported Φ, similar particles size	[21]

In this work, blue-emitting $Ca_{0.94}Eu_{0.06}MgSi_2O_6$ powders were synthesized through a co-precipitation method [23,24]. The powders were annealed with three different fluxes (NH_4F, NH_4Cl, or H_3BO_3). In our previous report [24], the $Ca_{0.94}Eu_{0.06}MgSi_2O_6$ powders formed submicrometer-sized particles having blue color with x = 0.14 and y = 0.05 on the CIE diagram, similar to those defined by the National Television System Committee color (0.14, 0.08), but the quantum efficiency was found to be low (Φ, ~5%). A low Φ is a drawback of nanocrystalline-sized phosphors; therefore, the main goal of this study was to improve the Φ using several different types of flux materials. NH_4F, NH_4Cl, and H_3BO_3 were selected as flux materials from the reported flux candidates [7–9,13–20] due to their low melting and boiling temperatures (Table 2), which are expected to decompose or evaporate during annealing process. Additionally, the large (>30%) ionic radii difference between the flux and the phosphor components indicates that flux contamination of the phosphor is unlikely to occur.

Table 2. Melting and boiling temperature of the fluxes.

Flux	Melting Point (°C)	Boiling Point (°C)
NH_4F	100	Decomposition *
NH_4Cl	338	Decomposition **
H_3BO_3	171	300 ***

* NH_4F (s) → NH_3 (g) + HF(g) > 100 °C, ** NH_4Cl (s) → NH_3 (g) + HCl (g) > 338 °C, *** H_3BO_3 (s) → B_2O_3 (s) + H_2O > 235 °C.

2. Experimental Procedure

2.1. Reagents

All chemicals were used without further purification and included tetraethyl orthosilicate (TEOS, 99.9%, Sigma Aldrich, St. Louis, MO, USA), $Mg(NO_3)_2{\cdot}6H_2O$ (98.3%, Fisher Scientific, Hampton, NH, USA), $Ca(NO_3)_2{\cdot}4H_2O$ (99.0%, Macron Fine Chemicals, Center Valley, PA, USA), Eu_2O_3 (99.99%, Alfa Aesar, Haverhill, MA, USA), nitric acid (69.3%, Fisher Scientific, Hampton, NH, USA), citric acid ($C_6H_8O_7{\cdot}H_2O$, ACS reagent grade, Macron Fine Chemicals, Center Valley, PA, USA), ethylene glycol (C_2H_6OH, certified, Fisher Scientific, Hampton, NJ, USA), polyethylene glycol (PEG, $C_2H_4O{\cdot}nH_2O$, molecular weight = 20,000 g/mol, Sigma Aldrich, St. Louis, MO, USA), ammonium hydroxide (28~30%, BDH Aristar Plus, Center Valley, PA, USA), NH_4F (96%, Alfa Aesar, Haverhill, MA, USA), NH_4Cl (ACS reagent grade, Macron Fine Chemicals, Center Valley, PA, USA), and H_3BO_3 (99.5%, Sigma Aldrich, St. Louis, MO, USA).

2.2. Preparation of $Ca_{0.94}Eu_{0.06}MgSi_2O_6$ with and without a Flux

The co-precipitation method was used to synthesize the powders by following previously reported procedures [23,24]. The concentration of 6 at.% Eu^{2+} activator was chosen as it is reported to have the highest photoluminescence (PL) emission intensity [24]. Tetraethyl orthosilicate (2.23 mL) was added to ethanol (20 mL) with several drops of nitric acid and deionized water while stirring for 30 min. Meanwhile, Eu_2O_3 (0.0015 mol) was dissolved in nitric acid (0.4 mL) solution to form aqueous $Eu(NO_3)_3$ solution. $Mg(NO_3)_2{\cdot}6H_2O$ (0.005 mol) and $Ca(NO_3)_2{\cdot}4H_2O$ (0.0047 mol) were dissolved in deionized water with stirring. After the two nitrate solutions became transparent, all three solutions (tetraethyl orthosilicate, $Eu(NO_3)_2$, and $Mg(NO_3)_2$ with $Ca(NO_3)_2$) were mixed together and then stirred for 1 h. Subsequently, ammonium hydroxide was added dropwise into the solution to reach a pH of 10 and initiate precipitation. White precipitates were formed, and the suspension was stirred for 8 h. Next, NH_4F, NH_4Cl, or H_3BO_3 was added to the solution at amounts of 2 wt.%, 6 wt.%, or 10 wt.% of $Ca_{0.94}Eu_{0.06}MgSi_2O_6$. The conversion of wt.% to mol.% for each flux is shown in Table 3. The solutions were then centrifuged and dried at 80 °C for 12 h. Finally, a post-synthesis annealing step was performed at 1100 °C for 2 h in air and then at 1100 °C for 4 h in a 5% H_2/95% N_2 atmosphere to transform Eu^{3+} to Eu^{2+}.

Table 3. Conversion of wt.% to mol.% for each flux in the solid phosphor powders.

wt.% Flux	NH_4F (mol.%)	NH_4Cl (mol.%)	H_3BO_3 (mol.%)
2	12	8	7
6	28	22	19
10	40	31	28

2.3. Characterization

The powders were analyzed by X-ray diffraction (XRD) on a D2 Phaser (Bruker, Karlsruhe, Germany) using CuKα radiation and a step size of 0.014° over a 2θ range of 20 to 80°. The crystallite sizes, lattice parameters, and ratio of the phases presented were calculated by Rietveld refinement using the TOPAS 4.2 software (Bruker). The sizes of the powders were examined by dynamic light scattering (DLS) on a Nanotrac Wave II system (Microtrac Inc., York, PA, USA) [25–27]. Particles were distributed in an aqueous solution by sonication in a water bath for DLS experiments. A field emission scanning electron microscope (FESEM, XL30, Philips, Amsterdam, Netherlands) at 10 keV was used to image the powders to confirm sizes and determine morphology. Samples were coated with iridium at 85 μA for 10 s before imaging. Energy dispersive spectroscopic analysis (EDS) was performed with a scanning electron microscope (Apreo SEM, FEI, Hillsboro, OR, USA) to analyze the concentration of elements. Absolute quantum efficiency (Φ) measurements were performed using an integrating sphere system, with sodium salicylate (Φ = 44%) as a reference standard. PL emission and excitation spectra were acquired with a fluorescence spectrophotometer (Hitachi F-7000, Hitachi High-Technologies Corporation, Tokyo, Japan) using λ = 350 nm excitation wavelength (pulse = 0.025 s). This excitation wavelength was selected as it produced the highest PL emission intensity for $Ca_{0.94}Eu_{0.06}MgSi_2O_6$ [24].

3. Results and Discussion

3.1. Crystal Structure and Lattice Parameters

Figure 1 shows the crystal structure of $CaMgSi_2O_6$. Also known as diopside, it has a monoclinic crystal structure with space group C2/c. The lattice parameters are a = 0.9743 nm, b = 0.8879 nm, c = 0.5230 nm, and β = 105.53° [24]. The coordination numbers for Ca^{2+}, Mg^{2+}, and Si^{4+} of 8, 6, and 4, respectively. The ionic radii of the ions are listed in Table 4. The radii differences between ions in $CaMgSi_2O_6$ and the flux are Mg^{2+}-B^{3+} = 90%, Si^{4+}-B^{3+} = 81%, O^{2-}-F^- = 5% (4-coordinated, 6-coordinated), O^{2-}-Cl^- = 26% (6-coordinated). The F^- from NH_4F and Cl^- from NH_4Cl are likely to be composed to HF (g) and HCl (g) during the annealing process (Table 2) although the radii difference between O^{2-} and F^-/or Cl^- is less than 30%. H^+ may occupy interstitial sites in the lattice because of its small size. Eu^{3+} (0.107 nm for 8-coordinated) is expected to occupy the Ca^{2+} sites due to the radii size similarity (5% difference) before reduction annealing and transforms to Eu^{2+} after reduction.

Table 4. The ionic radii (nm) of ions of in $CaMgSi_2O_6$ and fluxes, NH_4F, NH_4Cl, H_3BO_3.

Ions	4-Coordinated	6-Coordinated	8-Coordinated
Ca^{2+}	-	-	0.112
Mg^{2+}	-	0.072	-
Si^{4+}	0.026	-	-
O^{2-}	0.138	0.140	0.142
B^{3+}	0.011	0.027	-
F^-	0.131	0.133	-
Cl^-	-	0.181	-

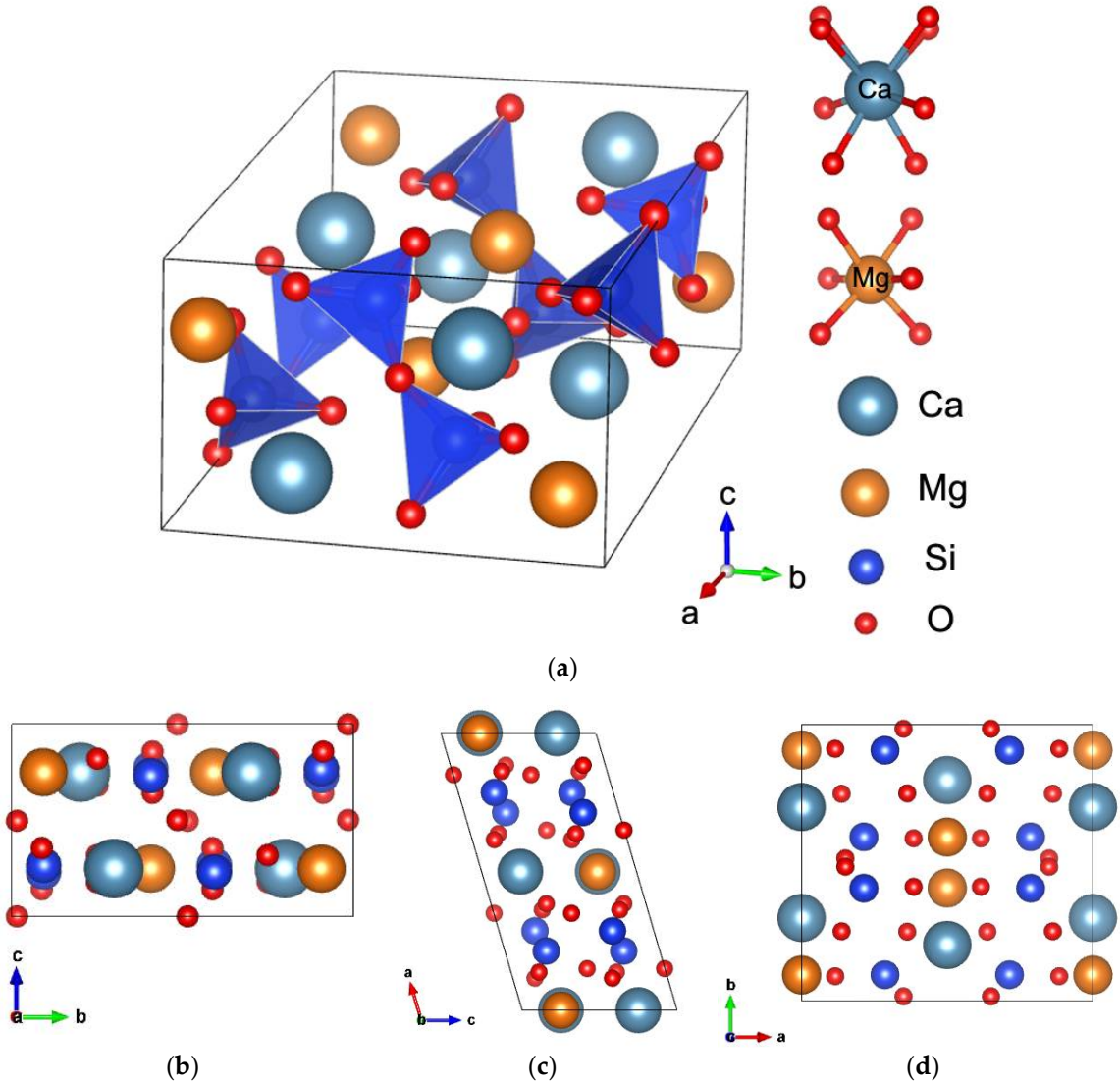

Figure 1. The crystal structure of $CaMgSi_2O_6$: (**a**) 3-D unit cell representation; (**b**) along the [100]; (**c**) along the [010]; and (**d**) along the [001] drawn by VESTA (Visualization for Electronic and Structural Analysis) [28].

XRD patterns of $Ca_{0.94}Eu_{0.06}MgSi_2O_6$ with and without NH_4F and NH_4Cl fluxes are shown in Figure 2. The peak widths narrowed with an increase in the concentration of NH_4F (Figure 2a), indicating an increase in crystallite size. Several small peaks from $CaEu_4(SiO_4)_3O$ were recorded for 10 wt.% NH_4F. $CaEu_4(SiO_4)_3O$ was previously identified in $Ca_{0.94}Eu_{0.06}MgSi_2O_6$ under annealing temperature of 1247 °C [29], which is a higher temperature than used in the present study, with no flux. As shown previously, a flux can decrease the temperature for the crystallization of phosphor materials [7,13], so that excessive NH_4F may lead to the new formation of $CaEu_4(SiO_4)_3O$ at the lower temperature by reducing the corresponding formation temperature. For the diffraction patterns from the powders prepared using NH_4Cl flux, shown in Figure 2b, the peak width also slightly narrowed with the increase of concentration of NH_4Cl. However, this narrowing is less pronounced in comparison with the NH_4F, indicating that the crystallite sizes with NH_4F flux were larger. The crystallite sizes for different concentrations of NH_4F and NH_4Cl fluxes are shown in Figure 2c. For the NH_4F flux, the crystallite size increased from roughly 13 nm with no flux to about 31 nm with 10 wt.% NH_4F. The maximum crystallite size for NH_4Cl flux was about 19 nm with 2 wt.% NH_4Cl. Different diffusion rates of the reactants through a flux may explain why the material produced with

NH_4F flux shows enlarged crystallite sizes compared to that made with NH_4Cl flux. Ions move through liquid flux during the annealing process with a diffusion coefficient expressed by $D = (1/f)\cdot kT$, where f is the frictional coefficient, k is the Boltzmann's constant, and T is the absolute temperature. The frictional coefficient can be expressed by $f = \pi\mu r$, where μ is viscosity and r is the radius of the ion. Therefore, a relationship $D \propto 1/r$ is found. F^- (0.119 nm) is smaller than Cl^- (0.167 nm), therefore NH_4F may act as a more effective flux compared to NH_4Cl from the point of view of enhanced diffusivity, assuming equivalent viscosities.

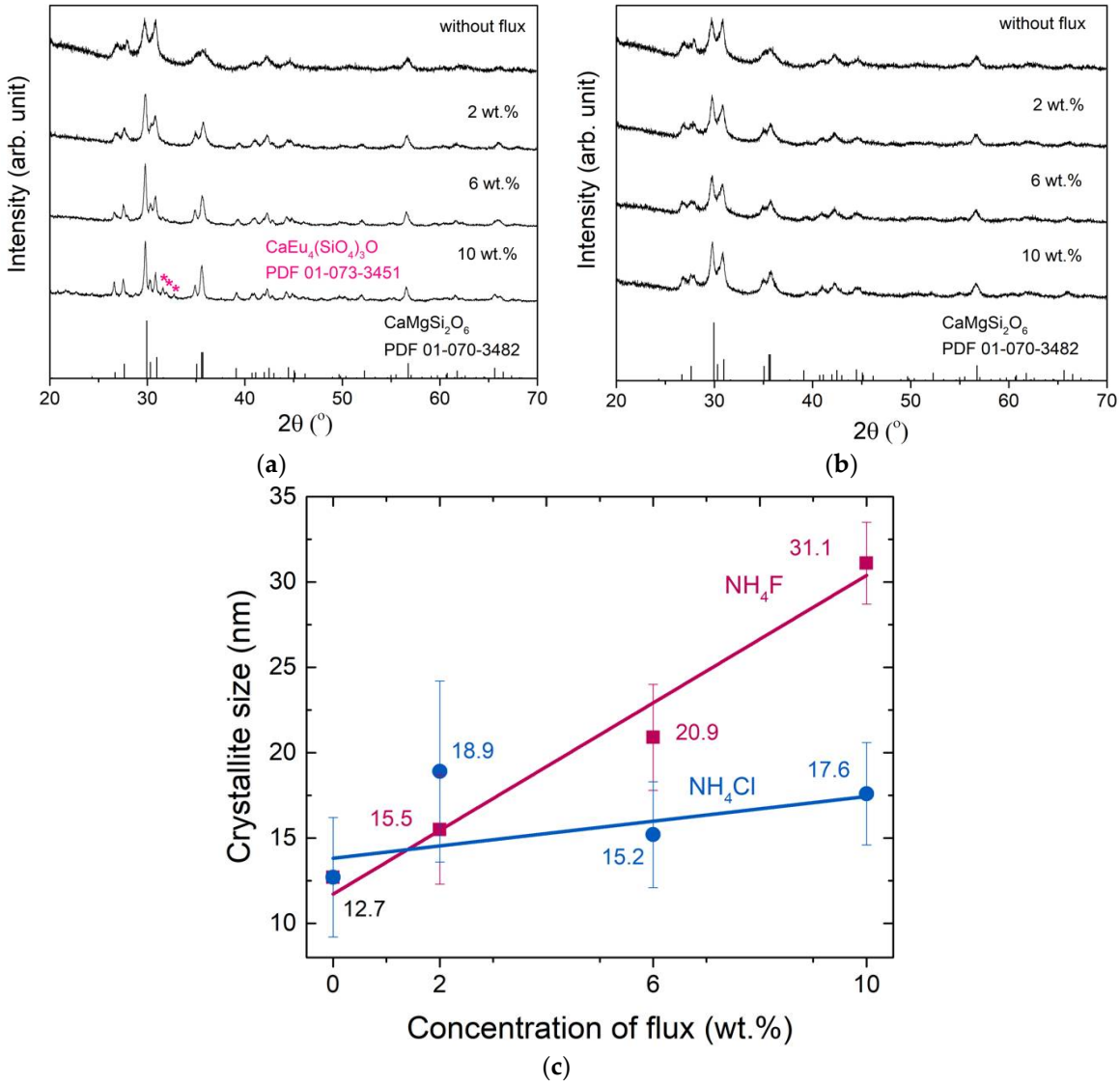

Figure 2. X-ray diffraction patterns of $Ca_{0.94}Eu_{0.06}MgSi_2O_6$ with a flux of (**a**) NH_4F and (**b**) NH_4Cl. (**c**) Calculated crystallite sizes of $Ca_{0.94}Eu_{0.06}MgSi_2O_6$ with NH_4F and NH_4Cl fluxes.

With the H_3BO_3 flux, SiO_2 impurities were detected, as shown in the XRD patterns in Figure 3a. Even though B^{3+} and Si^{4+} have quite different ionic radii (0.026 nm and 0.011 nm) [30], a substitution of B^{3+}on Si^{4+} sites on the tetrahedral site has been previously reported [31,32] although there is a charge difference between B^{3+} and Si^{4+}. Marler et al. [31] reported synthetic tourmaline (olenite) to replace partial silicon ions with excessive boron ions; and the difference in charge between Si^{4+} and B^{3+} was compensated by protons leading to the unusually high water content. Xia et al. [32] studied $La_5(Si_{2-x}B_{1-x})(O_{13-x}N_x):Ce^{3+}$ by replacing partially B^{3+} - O^{2-} by the Si^{4+} - N^{3-}; and the

charge difference from the replacement of B^{3+} by Si^{4+} was compensated by the substitution of O^{2-} by N^{3-}. In the current study, the charge difference from the partial replacement of Si^{4+} by B^{3+} could be compensated to produce oxygen vacancies due to no other ion replacements.

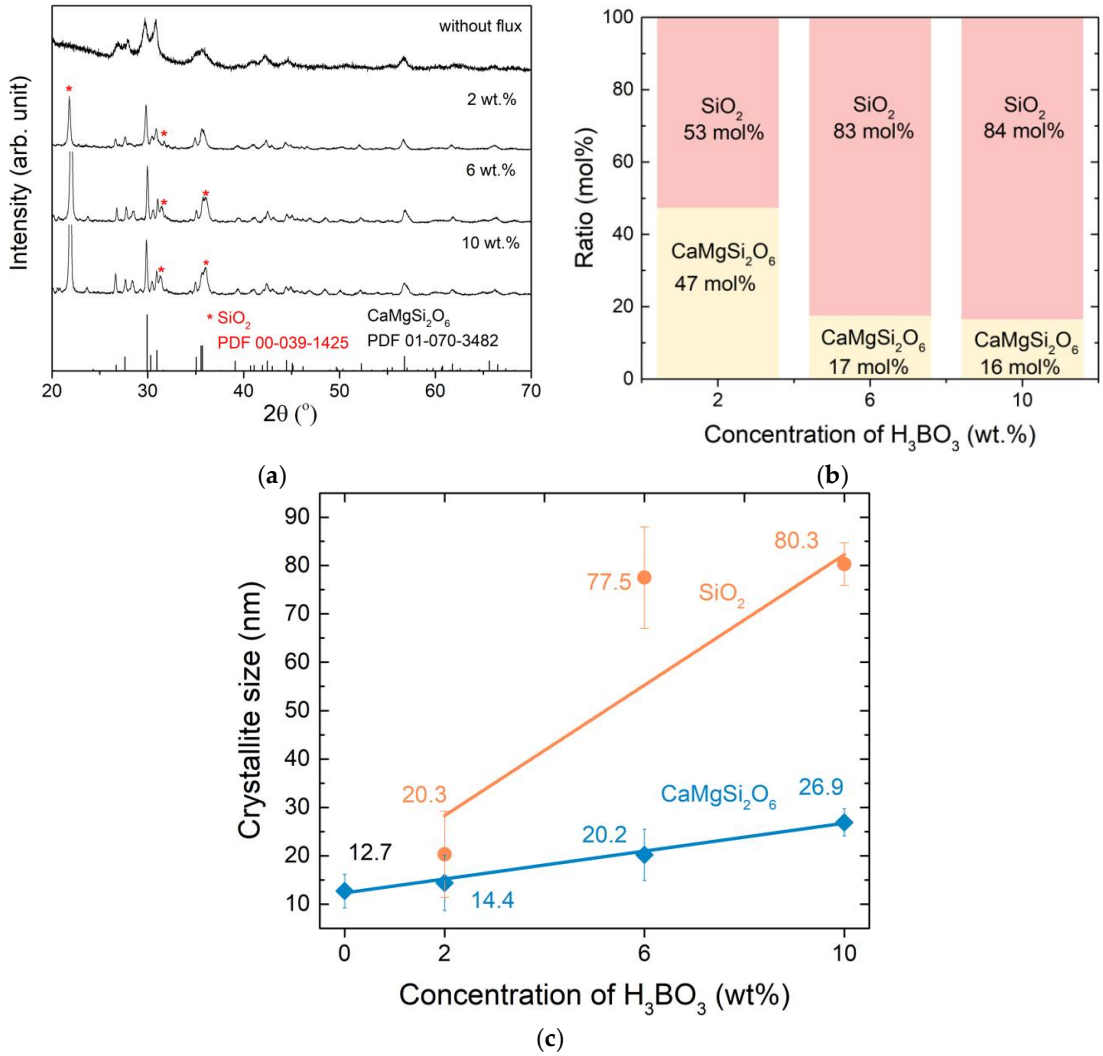

Figure 3. (**a**) X-ray diffraction patterns of $Ca_{0.94}Eu_{0.06}MgSi_2O_6$ with H_3BO_3 flux; (**b**) Calculated molar ratios of the phases present and (**c**) calculated crystallite sizes.

With an assumption that B ions partially replace the Si ions, the corresponding chemical reaction is:

$$CaMgSi_2O_6 + xH_3BO_3 \rightarrow CaMg(Si_{1-x/2}B_{x/2})_2O_6 + xSiO_2 + xH_2O + x/2H_2. \quad (1)$$

As the amount of H_3BO_3 increased (2–10 wt.%), the corresponding amount of SiO_2 increased (53–84 mol.%, Figure 3b). The crystallite size of the phosphor increased from ~13 nm to ~27 nm, while for SiO_2 it increased from 20 nm to 80 nm (Figure 3c).

The calculated lattice parameters of $Ca_{0.94}Eu_{0.06}MgSi_2O_6$ with and without each flux are shown in Figure 4. The lattice parameters of powders prepared with NH_4F and NH_4Cl (Figure 4a,b) were identical to the phosphors prepared without flux, indicating that these two fluxes did not affect the crystal structure of the resultant materials. In contrast, with H_3BO_3 flux, the *b* and *c* parameters did not show significant change, while *a* decreased from 0.9743 nm to 0.9670 nm. This is presumably due to the substitution of B^{3+} (0.011 nm) with Si^{4+} (0.036 nm) sites, causing the lattice parameter to decrease. Vegard's law [33], which is an empirical rule based on a linear relationship found between

lattice parameters and the size of the constituent elements. The formation of $\frac{1}{2}$O vacancies from the charge difference between Si^{4+} and B^{3+} can affect the lattice parameters. Therefore, the relationship between the initial lattice parameter and the one with B^{3+} is $a = a_0 - x(r_{Si} - r_B) - \frac{1}{2}xr_O$, where a is the lattice parameter (0.9670 nm) with 10 wt.% B^{3+} addition, a_0 is the initial lattice parameter (0.9743 nm), x is the partial substitution of B on Si, r_{Si}, r_B, r_O are the radii of Si^{4+}, B^{3+}, and O^{2-}, respectively. The x value obtained is 0.09, which is smaller than the molar fraction of H_3BO_3 added (0.28 converted from 10 wt.% H_3BO_3). The excess B^{3+} was not detected in the XRD patterns (detection limit of 3 ~5 wt.%). Therefore, due to the low boiling temperatures, it likely does not remain in the resultant powder. The change of lattice parameter *a,* while parameters *b* and *c* remain unchanged, can be explained by the ion arrangement. Along the [100] and [001] directions (see Figure 1b,d), there are two Si^{4+} along the *a*-axis, four along the *b*-axis, and three along *c*-axis. The fractions of one Si^{4+} along the *a*-, *b*-, and *c*-axes are 0.50, 0.25, and 0.33, respectively. The fraction of Si^{4+} along the *a*-axis is the largest, so that the replacement of Si^{4+} is affected more along this axis, resulting in a decrease of *a* with an addition of 10 wt.% H_3BO_3. Another possible reason for a change in lattice parameter of $Ca_{0.94}Eu_{0.06}MgSi_2O_6$ is H^+ dissolved in interstitial sites, but this would cause an increase of lattice parameters, which was not observed.

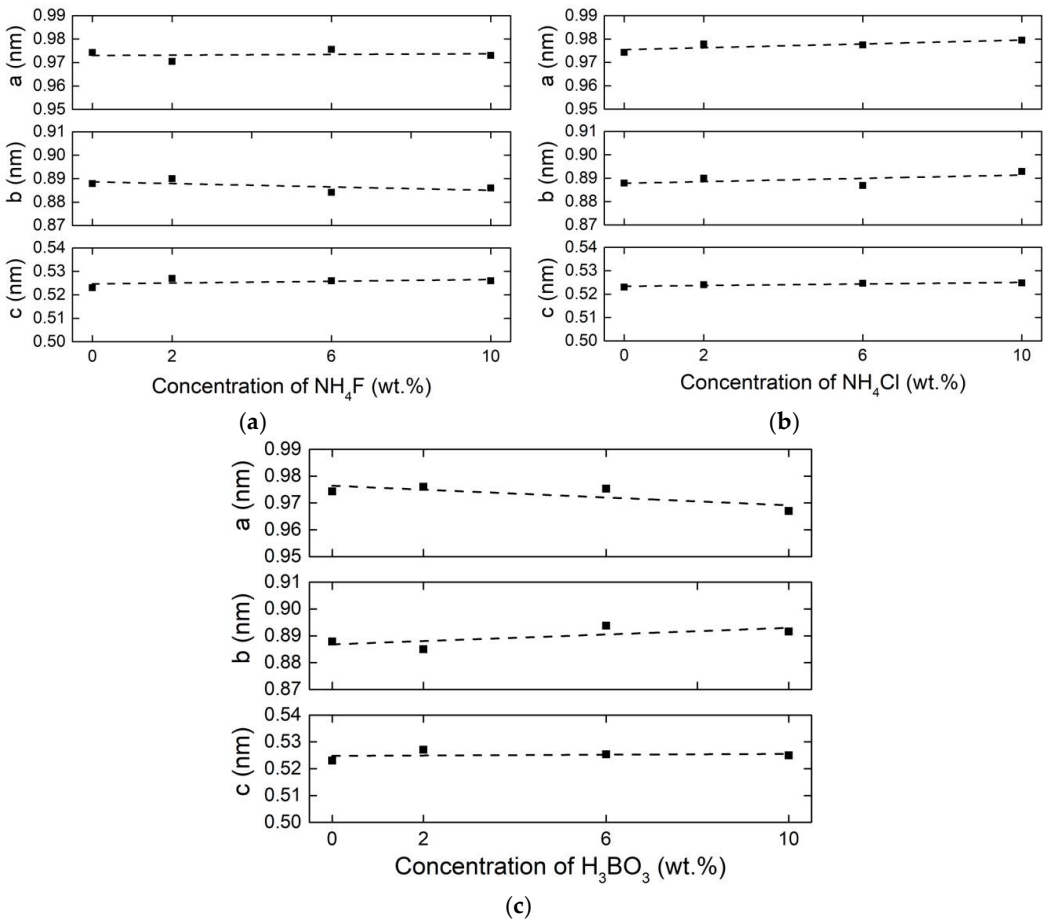

Figure 4. Calculated lattice parameters of $Ca_{0.94}Eu_{0.06}MgSi_2O_6$ from the X-ray diffraction results with a flux of (**a**) NH_4F; (**b**) NH_4Cl; and (**c**) H_3BO_3.

3.2. Scanning Electron Microscopy and Dynamic Lighting Scattering Analysis

SEM images of $Ca_{0.94}Eu_{0.06}MgSi_2O_6$ are shown in Figure 5a for no flux, Figure 5b–d for NH_4F flux addition, Figure 5e–g for NH_4Cl flux addition, and Figure 5h–j for H_3BO_3 flux addition. For NH_4F or NH_4Cl fluxes, the particle sizes and morphologies were similar to those without a flux. However,

the particles with the H_3BO_3 flux were aggregated, and the particle sizes were irregular. From EDS analysis, the ratio of Ca:Mg:Si:O was 1:1:7:13 in the large particles (yellow point in Figure 5h), where the amounts of Si and O are two to three times more than those of $CaMgSi_2O_6$ (Ca:Mg:Si:O = 1:1:2:6). In the small particles (red point in Figure 5h), the ratio of Ca:Mg:Si:O was 1:1:3:5, which is closer to that of $CaMgSi_2O_6$. Although the results from EDS are considered more accurate for polished surfaces than the powders, the ratio of Ca, Mg, Si, O demonstrated differences between small and large particles. Also, given that the EDS analysis penetrates 1–2 μm below the surface [34], $CaMgSi_2O_6$ could be detected under the SiO_2 particles, which could be the reason EDS analysis showed a small amount of Ca and Mg, when presumably large SiO_2 particles were analyzed. Therefore, large particles can be considered as SiO_2 and the aggregated, small particles as $CaMgSi_2O_6$.

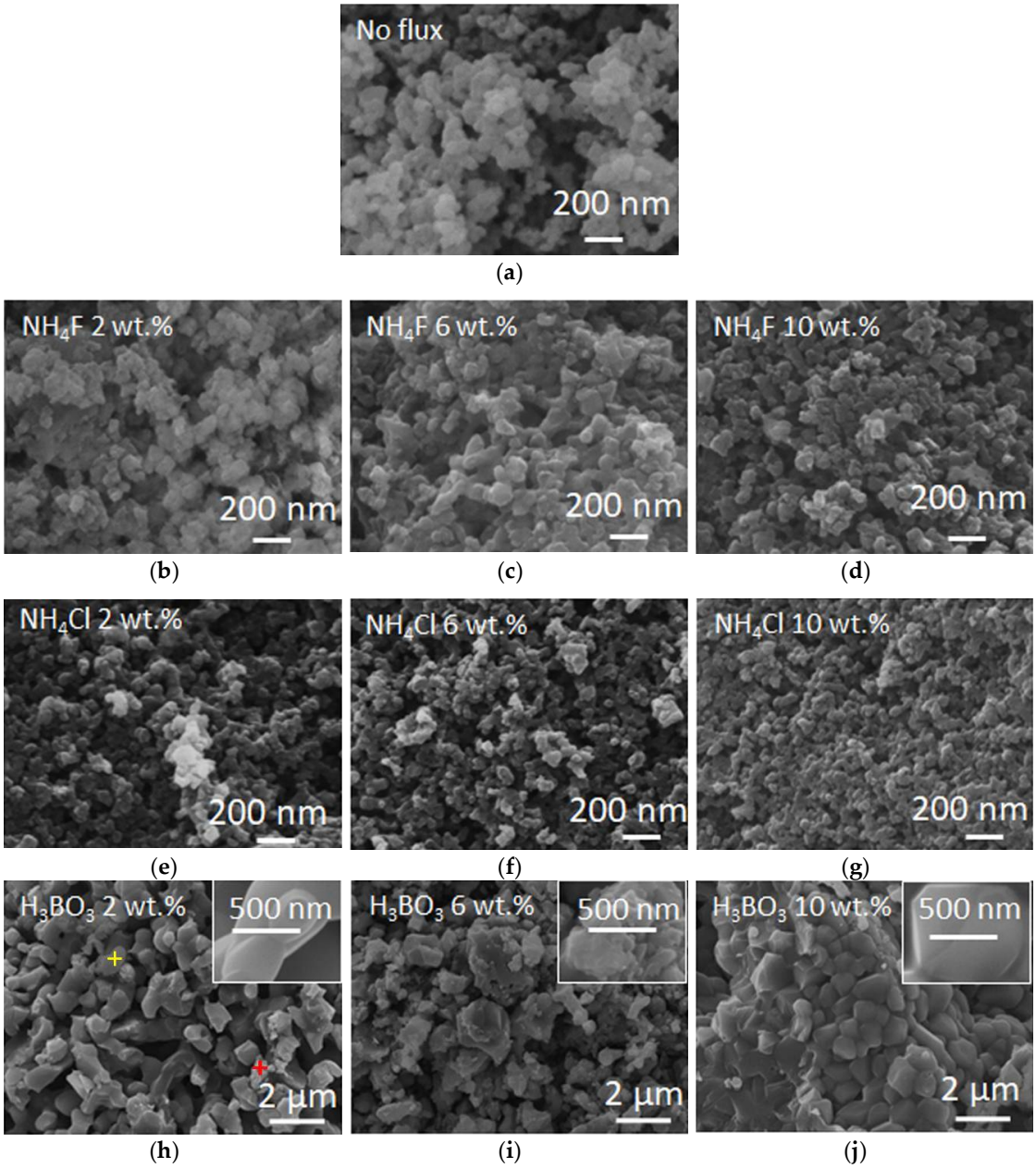

Figure 5. Scanning electron microscopy images of $Ca_{0.94}Eu_{0.06}MgSi_2O_6$. Without any flux (**a**) taken from [24]. With NH_4F flux (**b**) 2 wt.%, (**c**) 6 wt.%, and (**d**) 10 wt.%. With NH_4Cl flux: (**e**) 2 wt.%, (**f**) 6 wt.%, and (**g**) 10 wt.%. With H_3BO_3 flux: (**h**) 2 wt.%, (**i**) 6 wt.%, (**j**) 10 wt.%.

From the DLS analysis (Figure 6), the average particle sizes were 83 nm for powders without flux. With the NH_4F flux, the average particles sizes were 80 nm (2 wt.%), 100 nm (6 wt.%), and 133 nm (10 wt.%), respectively. For the NH_4Cl flux, the corresponding particle sizes were found to be 84 nm (2 wt.%), 82 nm (6 wt.%), and 118 nm (10 wt.%). Overall, this indicates that particles were still submicron-sized with the addition of flux. However, some studies reported uniformly shaped and enlarged particles with up to 14 wt.% of flux addition [8,14,15,19]. For the H_3BO_3 flux, the average particle sizes were 307 nm (2 wt.%), 318 nm (6 wt.%), and 375 nm (10 wt.%), which resulted from an increase in the amount of the SiO_2 particles.

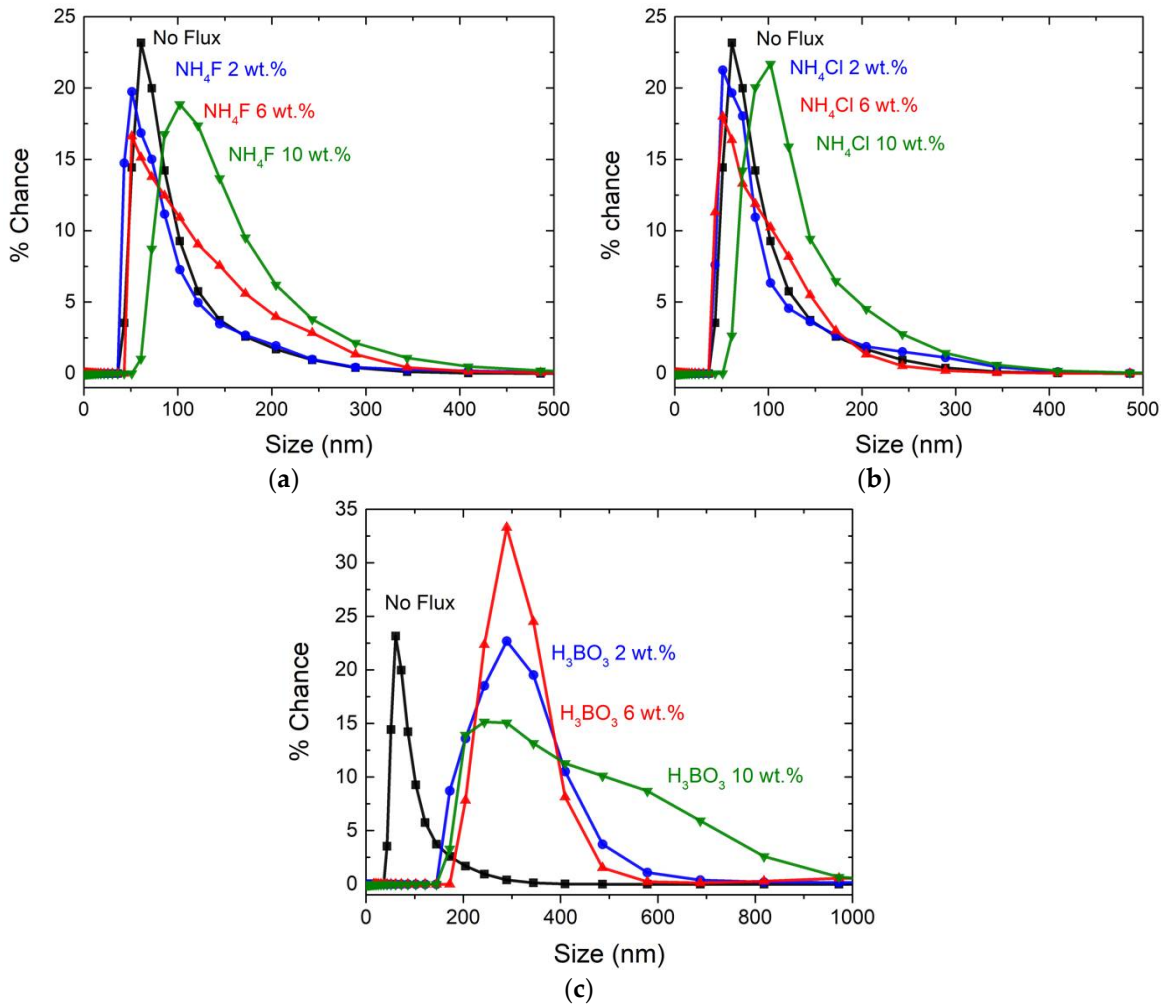

Figure 6. The distributions of particle sizes of $Ca_{0.94}Eu_{0.06}MgSi_2O_6$ with fluxes (**a**) NH_4F; (**b**) NH_4Cl and (**c**) H_3BO_3 analyzed by dynamic light scattering analysis.

3.3. Photoluminescence Spectra and Quantum Efficiency

The PL excitation (PLE) was monitored at 458 nm, and the PL emission spectra were obtained under λ_{ex} = 350 nm as an excitation wavelength. Although the Eu ions were introduced from a strong nitric acid solution during the synthetic process, this acid may cause traces of transition metal ions impurities (Cr, Cu, Pb, Ni, Zn, Au, Ti). However, these are negligible due to the very low concentration in the whole solution (<0.01 ppm). If all transition metals are present in the phosphor powders, the concentration would be ~0.1 ppb, which would not influence the luminescence properties. Figure 7a–c shows the PLE spectra (dashed lines) with a broadband absorption in the near UV region from 200 nm to 400 nm, with a maximum at 350 nm, which is attributed to the allowed transition of

Eu^{2+}. The PL emission (solid lines) shows a spectrum with a maximum at 458 nm, which corresponds to the parity allowed $4f^6 5d^1 \rightarrow 4f^7$ transition of Eu^{2+}. In Figure 7a, the absorption and emission intensities, together with the quantum efficiency (Φ), increased with the increase of the amount of NH_4F. A maximum Φ of 17% was found at 11 wt.% of NH_4F. For the NH_4Cl flux (Figure 7b), the quantum efficiency increased from 5% to 11% when 2 wt.% of NH_4Cl was added. For the amounts of NH_4Cl > 2 wt.%, Φ decreased. As shown in Figure 7c, Φ with H_3BO_3 was very low, ~1%, because of the significant amount of SiO_2 in the sample, as was confirmed by the XRD (Figure 3b). Figure 7d is a plot of Φ as a function of the amount of flux for all three fluxes used in the current study. A cumulative analysis of Figures 2c and 7d demonstrates that the change in the crystallite sizes of the materials produced with NH_4F and NH_4Cl fluxes, directly relates to the change in their corresponding quantum efficiencies [35]. For 0–10 wt.% of NH_4F, the average crystallite size increased from 13 nm to 31 nm, and the corresponding quantum efficiencies improved from 5% to 17%. Similarly, for 0 wt.%, 2 wt.%, 6 wt.%, and 10 wt.%, of the NH_4Cl flux, the average crystallite sizes were 13 nm, 19 nm, 15 nm, 18 nm, respectively, and the corresponding quantum efficiencies showed similar trend. In constant, with 0–10 wt.% of H_3BO_3, the crystallite size increased from ~13 nm to ~27 nm, but the quantum efficiency was low due to the presence of a large fraction of the secondary phase, SiO_2.

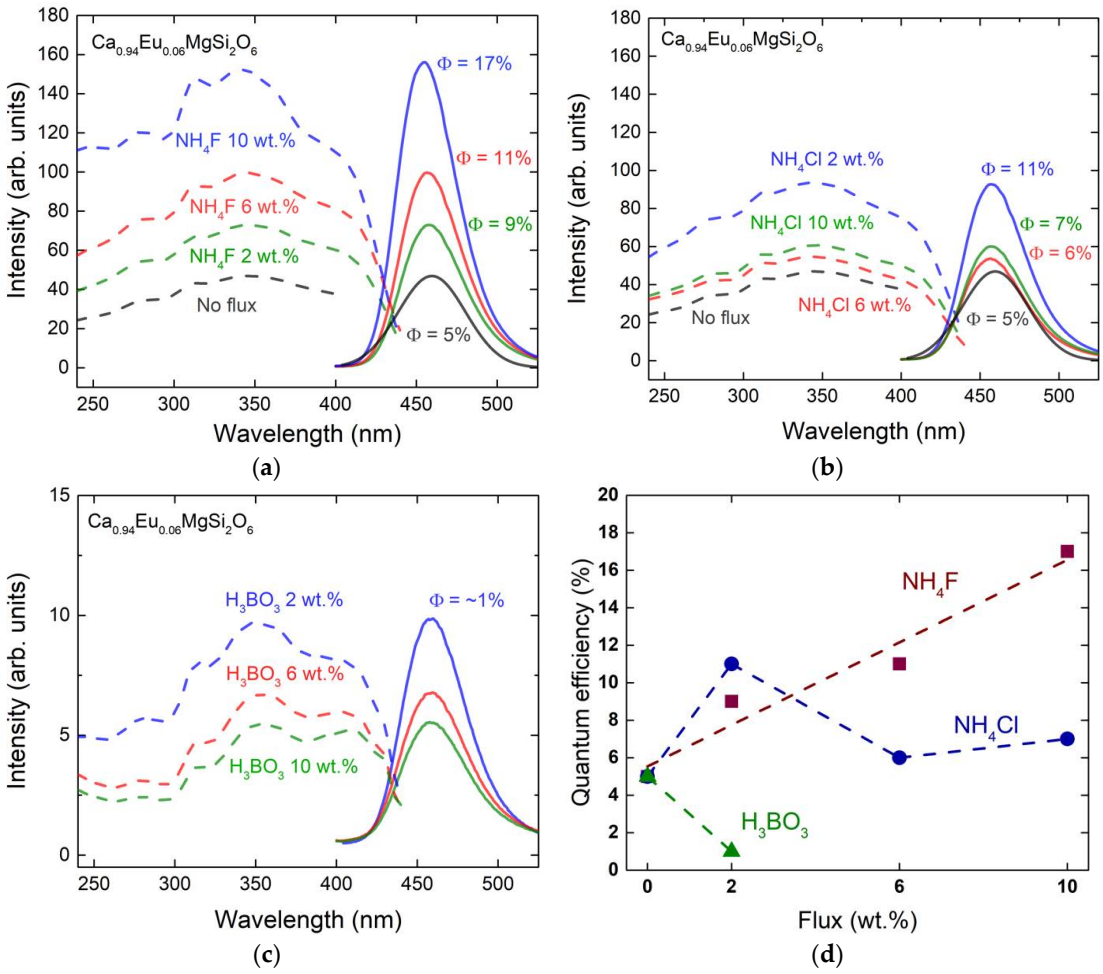

Figure 7. Photoluminescence excitation (dashed line monitored at 458 nm) and emission (solid line, λ_{ex} = 350 nm) spectra of $Ca_{0.94}Eu_{0.06}MgSi_2O_6$ with (**a**) NH_4F (no flux, 2 wt.%, 6 wt.%, and 10 wt.%); (**b**) NH_4Cl (no flux, 2 wt.%, 6 wt.%, and 10 wt.%); (**c**) H_3BO_3 (2 wt.%, 6 wt.%, and 10 wt.%). Φ = quantum efficiency; (**d**) The relationship between quantum efficiency and the amount of flux.

3.4. Effect of High Concentration of NH_4Cl

Increased amount of NH_4Cl was examined to determine if the high concentration of this particular flux resulted in the formation of second phase, a change in crystal structure, or further improvement of Φ while phosphors with NH_4F and H_3BO_3 already consist of secondary phases below 10 wt.% of the flux. Figure 8a shows the XRD patterns of $CaMgSi_2O_6$ produced with 14, 17, and 20 wt.% of NH_4Cl flux. There were no secondary phases with 14 and 17 wt.%, but $CaSiO_3$ was detected for 20 wt.% of NH_4Cl. The lattice parameters *a* and *c* were not affected, but *b* decreased from 0.8867 nm (for 14 wt.%) to 0.8852 nm (for 20 wt.%) (Figure 8b). Given that the radii difference between Cl^- and O^{2-} is 26%, excessive Cl^- may substitute for O^{2-} and produce a charge imbalance. This could cause cation defects and/or the creation of secondary phases such as $CaSiO_3$. $MgSiO_3$ could also potentially be produced due to the substitution O^{2-} by Cl^-, but it was not detected by XRD. Vegard's law can also be applied to the *b*–axis change, with an assumption that there are vacancy defects of $\frac{1}{2}$ Ca^{2+}, $\frac{1}{2}$ Mg^{2+} or $\frac{1}{4}$ Si^{4+} due to the charge difference between O^{2-} and Cl^-. To obtain the maximum difference between *b* and b_0, Ca^{2+} vacancies were assumed. The lattice parameter change is $b = b_0 - \frac{1}{2}xr_{Ca} - x(r_O - r_{Cl})$, where *b* is the lattice parameter (0.8852 nm) with 20 wt.% Cl^- additions, b_0 is the initial lattice parameter with no flux (0.8900 nm), *x* is the partial substitution of Cl^- on O^{2-}, and r_{Ca}, r_{Si}, r_O, r_{Cl} are radii of Ca^{2+}, Si^{4+}, O^{2-}, and Cl^-, respectively. The obtained *x* value is 0.32, which is smaller than the molar fraction of Cl^- in $CaMgSi_2O_6$ (0.50, converted from 20 wt.% NH_4Cl). The remaining Cl^- is likely from the excessive addition of NH_4Cl. The crystal structure along the [001] (Figure 1d) and [010] (Figure 1c) directions shows one Ca^{2+} and one Mg^{2+} along the *a*- and *c*-axes and two Ca^{2+} and two Mg^{2+} along the *b*-axis, resulting in the fraction of Mg^{2+} and Ca^{2+} along the *b*-axis being twice higher than that along the *a*- and *c*-axes. Therefore, the *b*-axis was altered more than the *a*- and *c*-axes.

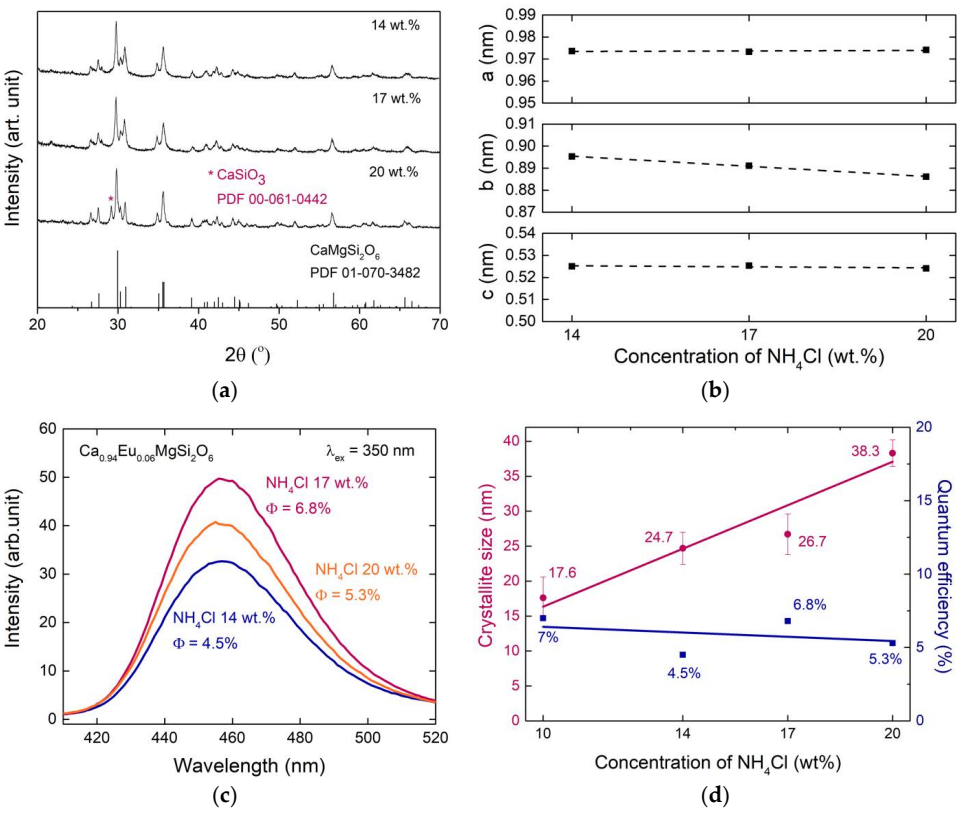

Figure 8. Effect of additional NH_4Cl flux (14 wt.%, 17 wt.%, and 20 wt.%) on $CaMgSi_2O_6$:Eu^{2+}. (**a**) X-ray diffraction patterns; (**b**) calculated lattice parameters of $CaMgSi_2O_6$:Eu^{2+}; (**c**) photoluminescence emission spectra (λ_{ex} = 350 nm) and quantum efficiencies (**d**) calculated crystallite sizes (pink color) and quantum efficiencies (blue color) from 0 to 20 wt.% NH_4Cl.

The PL emission spectra and Φs with additional NH_4Cl flux are shown in Figure 8c. The Φs were not significantly changed with an increase in the amount of NH_4Cl. A comparison between crystallite size and Φs with the amount of NH_4Cl flux is shown in Figure 8d. The maximum Φ corresponded to 2 wt.%; over 2 wt.% Φ initially decreased and eventually leveled off. However, the crystallite sizes increased with an increase in the concentration of the flux. This implies that the flux, although increasing the crystallite size, also changed lattice parameters resulting in no enhancement of Φ due to the inappropriate amount of flux addition.

4. Conclusions

The crystallite size and quantum efficiency of blue-emitting $Ca_{0.94}Eu_{0.06}MgSi_2O_6$ submicrometer-sized phosphors prepared by the co-precipitation method were altered with the addition of a flux, NH_4F, NH_4Cl, or H_3BO_3. The particle sizes both with and without fluxes (NH_4F or NH_4Cl) were submicrometer-sized (~100 nm). A direct correlation between crystallite sizes of the materials produced with NH_4F or NH_4Cl fluxes and their corresponding quantum efficiencies was verified. For the NH_4F flux, the crystallite size increased from 13 nm (no flux) to 31 nm (10 wt.% flux). The corresponding quantum efficiencies improved from 5% (no flux) to 17% (10 wt.% flux), correlating with the increase in crystallite size. For the NH_4Cl flux, the crystallite sizes increased to 18 nm with 10 wt.% from 13 nm with no flux, with a corresponding increase in quantum efficiency from 5% to 11%. This demonstrates that NH_4Cl is not an effective flux, likely due to its lower liquid diffusion coefficient compared to NH_4F. Additionally, it was shown that further increasing the amount of the NH_4Cl flux (14–20 wt.%) only slightly improved the corresponding quantum efficiency. The H_3BO_3 flux produced a substantial amount of SiO_2 as a secondary phase, which negatively affected the quantum efficiency of the resultant material. From lattice parameter measurements, it is shown that the phosphor was contaminated with boron ions, and silicon was leached out of the lattice.

In summary, it is shown that the poor quantum efficiency of submicron-sized phosphors can be improved by using NH_4F flux for $CaMgSi_2O_6$:Eu^{2+}, but the flux composition and amount must be carefully assessed to evaluate the presence of secondary phases.

Author Contributions: Conceptualization, J.H. and J.M.; Methodology, J.H., C.Z.; Software, J.H.; Validation, E.N., O.A.G., and J.M.; Formal Analysis, J.H., E.N., R.E.R., and J.M.; Investigation, J.M.; Resources, O.A.G., G.A.H., J.M.; Data Curation, J.H., E.N., J.M.; Writing-Original Draft Preparation, J.H.; Writing-Review & Editing, E.N., O.A.G., and J.M.; Visualization, J.H.; Supervision, J.M.; Project Administration, J.M.; Funding Acquisition, J.M.

Funding: This research was funded by [the National Science Foundation, Ceramics Program] grant number [Grant DMR-1411192].

Acknowledgments: This work is supported by the National Science Foundation, Ceramics Program Grant DMR-1411192. This work was performed in part at the San Diego Nanotechnology Infrastructure (SDNI) of UCSD, a member of the National Nanotechnology Coordinated Infrastructure, which is supported by the National Science Foundation (Grant ECCS-1542148).

Conflicts of Interest: The authors declare no conflicts of interest.

References

1. Blasse, G.; Grabmaier, B.C. *Luminescent Materials*; Springer: Berlin/Heidlberg, Germany, 1994.
2. Han, J.K.; Choi, J.I.; Piquette, A.; Hannah, M.; Anc, M.; Galvez, M.; Talbot, J.B.; McKittrick, J. Phosphor development and integration for near-UV LED solid state lighting. *ECS J. Solid State Sci. Technol.* **2012**, *2*, R3138–R3147. [CrossRef]
3. Luo, H.; Liu, J.; Zheng, X.; Han, L.; Ren, K.; Yu, X. Enhanced photoluminescence of Sr_3SiO_5:Ce^{3+} and tuneable yellow emission of Sr_3SiO_5:Ce^{3+}, Eu^{2+} by Al^{3+} charge compensation for W-LEDs. *J. Mater. Chem.* **2012**, *22*, 15887–15893. [CrossRef]
4. Lee, S.H.; Choi, J.I.; Kim, Y.J.; Han, J.K.; Ha, J.; Novitskaya, E.; Talbot, J.B.; McKittrick, J. Comparison of luminescent properties of Y_2O_3:Eu^{3+} and $LaPO_4$:Ce^{3+}, Tb^{3+} phosphors prepared by various synthetic methods. *Mater. Charact.* **2015**, *103*, 162–169. [CrossRef]

5. Terraschke, H.; Wickleder, C. UV, blue, green, yellow, red, and small: Newest developments on Eu-doped nanophosphors. *Chem. Rev.* **2015**, *115*, 11352–11378. [CrossRef] [PubMed]
6. Jung, K.Y.; Lee, C.H.; Kang, Y.C. Effect of surface area and crystallite size on luminescent intensity of Y_2O_3:Eu phosphor prepared by spray pyrolysis. *Mater. Lett.* **2005**, *59*, 2451–2456. [CrossRef]
7. Chiang, C.H.; Liu, T.H.; Lin, H.Y.; Kuo, H.Y.; Chu, S.Y. Effects of flux additives on the characteristics of $Y_{2.95}Al_5O_{12}$:0.05Ce^{3+} phosphor: Particle growth mechanism and luminescence. *J. Appl. Phys.* **2013**, *114*, 243517. [CrossRef]
8. Zhang, Q.; Ni, H.; Wang, L.; Xiao, F. Effects of BaF_2 flux on the synthesis of green emitting phosphor $CaSc_2O_4$:Ce^{3+}. *ECS J. Solid State Sci. Technol.* **2014**, *4*, R23–R26. [CrossRef]
9. Dai, P.; Zhang, X.; Sun, P.; Yang, J.; Wang, L.; Yan, S.; Liu, Y.; Ballato, J. Influence of flux on morphology and luminescence properties of phosphors: A case study on $Y_{1.55}Ti_2O_7$:0.45Eu^{3+}. *J. Am. Ceram. Soc.* **2012**, *95*, 1447–1453. [CrossRef]
10. Lee, G.-H.; Yoon, C.; Kang, S. Role of flux in the production process of red phosphors for white LEDs. *J. Mater. Sci.* **2008**, *43*, 6109–6115. [CrossRef]
11. Pamplin, B.R. *Crystal Growth*, 2nd ed.; Pergamon Press: Beccles/London, UK, 1980.
12. Stoll, S.L.; Stacy, A.M. Single-crystal growth, alkali metal ordering, and superconductivity in $La_{2-x}M_xCuO_4$ (M = Na, K). *Inorg. Chem.* **1994**, *33*, 2761–2765. [CrossRef]
13. Chen, Y.B.; Gong, M.L.; Cheah, K.W. Effects of fluxes on the synthesis of $Ca_3Sc_2Si_3O_{12}$:Ce^{3+} green phosphors for white light-emitting diodes. *Mater. Sci. Eng. B Adv. Funct. Solid State Mater.* **2010**, *166*, 24–27. [CrossRef]
14. Tang, J.Y.; He, Y.M.; Hao, L.Y.; Xu, X.; Agathopoulos, S. Fine-sized $BaSi_3Al_3O_4N_5$:Eu^{2+} phosphors prepared by solid-state reaction using BaF_2 flux. *J. Mater. Res.* **2013**, *28*, 2598–2604. [CrossRef]
15. Wang, X.; Li, J.H.; Shi, P.L.; Guan, W.M.; Zhang, H.Y. High dispersibility and enhanced luminescence properties of $BaMgAl_{10}O_{17}$:Eu^{2+} phosphors derived from molten salt synthesis. *Opt. Mater.* **2015**, *46*, 432–437. [CrossRef]
16. Liu, J.Q.; Wang, X.J.; Xuan, T.T.; Wang, C.B.; Li, H.L.; Sun, Z. $Lu_3(Al,Si)_5(O,N)_{12}$:Ce^{3+} phosphors with broad emission band and high thermal stability for white LEDs. *J. Lumin.* **2015**, *158*, 322–327. [CrossRef]
17. Dong, K.; Li, Z.L.; Xiao, S.G.; Xiang, Z.F.; Zhang, X.A.; Yang, X.L.; Jin, X.L. Yellowish-orange luminescence in $Sr_8Al_{12}O_{24}S_2$:Eu^{2+} phosphor. *J. Alloys Compd.* **2012**, *543*, 105–108. [CrossRef]
18. Lee, S.H.; Jung, D.S.; Han, J.M.; Koo, H.Y.; Kang, Y.C. Fine-sized $Y_3Al_5O_{12}$:Ce phosphor powders prepared by spray pyrolysis from the spray solution with barium fluoride flux. *J. Alloys Compd.* **2009**, *477*, 776–779. [CrossRef]
19. Kang, H.S.; Kang, Y.C.; Jung, K.Y.; Park, S.B. Eu-doped barium strontium silicate phosphor particles prepared from spray solution containing NH_4Cl flux by spray pyrolysis. *Mater. Sci. Eng. B Solid State Mater. Adv. Technol.* **2005**, *121*, 81–85. [CrossRef]
20. Wang, J.S.; Zhu, D.-C.; Zheng, Q.; Han, T. Effect of flux on the composition and luminescent properties of $Ca_{0.68}Mg_{0.2}SiO_3$:0.12Eu^{3+} red phosphor. *J. Lumin.* **2016**, *179*, 183–188. [CrossRef]
21. Zhang, B.; Feng, L.; Qiang, Y. Preparation and photoluminescence properties of the $Sr_{1.56}Ba_{0.4}SiO_4$:0.04Eu^{2+} phosphor. *J. Lumin.* **2012**, *132*, 1274–1277. [CrossRef]
22. Pires, A.M.; Davolos, M.R. Luminescence of europium (III) and manganese (II) in barium and zinc orthosilicate. *Chem. Mater.* **2001**, *13*, 21–27. [CrossRef]
23. Pawar, A.U.; Jadhav, A.P.; Pal, U.; Kim, B.K.; Kang, Y.S. Blue and red dual emission nanophosphor $CaMgSi_2O_6$:Eu^{n+}; crystal structure and electronic configuration. *J. Lumin.* **2012**, *132*, 659–664. [CrossRef]
24. Ha, J.; Wang, Z.; Novitskaya, E.; Hirata, G.A.; Graeve, O.A.; Ong, S.P.; McKittrick, J. An integrated first principles and experimental investigation of the relationship between structural rigidity and quantum efficiency in phosphors for solid state lighting. *J. Lumin.* **2016**, *179*, 297–305. [CrossRef]
25. Cahill, J.T.; Ruppert, J.N.; Wallis, B.; Liu, Y.; Graeve, O.A. Development of mesoporosity in scandia-stabilized zirconia: Particle size, solvent, and calcination effects. *Langmuir* **2014**, *30*, 5585–5591. [CrossRef] [PubMed]
26. Graeve, O.A.; Fathi, H.; Kelly, J.P.; Saterlie, M.S.; Sinha, K.; Rojas-George, G.; Kanakala, R.; Brown, D.R.; Lopez, E.A. Reverse micelle synthesis of oxide nanopowders: Mechanisms of precipitate formation and agglomeration effects. *J. Colloid Interface Sci.* **2013**, *407*, 302–309. [CrossRef] [PubMed]
27. Saterlie, H.S.M.S.; Kavlicoglu, B.; Liu, Y.; Graeve, O.A. Surfactant effects on dispersion characteristics of copper-based nanofluids: A dynamic light scattering study. *Chem. Mater.* **2012**, *24*, 3299–3306. [CrossRef]

28. Momma, K.; Izumi, F. VESTA: A three-dimensional visualization system for electronic and structural analysis. *J. Appl. Crystallogr.* **2008**, *41*, 653–658. [CrossRef]
29. Knyazev, A.V.; Bulanov, E.N.; Korshunov, A.O.; Krasheninnikova, O.V. Synthesis and thermal expansion of some lanthanide-containing apatites. *Inorg. Mater.* **2013**, *49*, 1133–1137. [CrossRef]
30. Shannon, R.D. Revised effective ionic radii and systematic studies of interatomie distances in halides and chaleogenides. *Acta Crystallogr. Sect. A Cryst. Phys. Diffr. Theor. Gen. Crystallogr.* **1976**, *32*, 751–767. [CrossRef]
31. Marler, B.; Borowski, M.; Wodara, U.; Schreyer, W. Synthetic tourmaline (olenite) with excess boron replacing silicon in the tetrahedral site: II. Structure analysis. *Eur. J. Mineral.* **2002**, *14*, 763–771. [CrossRef]
32. Xia, Z.; Molokeev, M.S.; Im, W.B.; Unithrattil, S.; Liu, Q. Crystal structure and photoluminescence evolution of $La_5(Si_{2+x}B_{1-x})(O_{13-x}N_x):Ce^{3+}$ solid solution phosphors. *J. Phys. Chem. C* **2015**, *119*, 9488–9495. [CrossRef]
33. Denton, A.R.; Ashcroft, N.W. Vegard's law. *Phys. Rev. A* **1991**, *43*, 3161–3164. [CrossRef] [PubMed]
34. Prencipe, D.D.I.; Zani, A.; Rizzo, D.; Passoni, M. Energy dispersive X-ray spectroscopy for nanostructured thin film density evaluation. *Sci. Technol. Adv. Mater.* **2015**, *16*, 025007. [CrossRef] [PubMed]
35. Dantelle, G.; Salaün, M.; Bruyère, R.; Kodjikian, S.; Ibanez, A. Luminescent coatings prepared from optimized YAG:Ce nanoparticles. *Thin Solid Films* **2017**, *643*, 36–42. [CrossRef]